RSC Advances

PAPER

View Article Online
View Journal | View Issue

Cite this: *RSC Adv.*, 2026, **16**, 29758

ZrO$_2$-embedded nitrogen-doped carbon-derived MOF/COF for supercapacitors

Hani Nasser Abdelhamid, *[a] Faisal K. Algethami [a] and Mervat Ibrahim *[b]

Porous materials, including hybrid materials (*e.g.*, metal–organic frameworks, MOFs) and pure organic materials (*e.g.*, covalent organic frameworks, COFs), were investigated for electrochemical energy storage. This study produced a hybrid material composed of UiO-66 MOF and a COF, which was subsequently carbonized at different temperatures to yield ZrO$_2$-embedded nitrogen-doped carbon for supercapacitor applications. The materials were analyzed using X-ray diffraction (XRD), X-ray photoelectron spectroscopy (XPS), Fourier-transform infrared spectroscopy (FT-IR), thermogravimetric analysis (TGA), scanning electron microscopy (SEM), and transmission electron microscopy (TEM). The results confirmed the synthesis of UiO-66@COF and the generation of ZrO$_2$@N-doped carbon through post-carbonization. Electrochemical experiments revealed that the carbonized composite exhibits enhanced capacitance performance compared with UiO-66 and COF materials. The UiO-66@COF_700 electrode showed a specific capacitance of 195 F/g at 1 A/g, remarkable rate capability, and stable cycling performance over 5000 cycles. The energy storage mechanism includes both capacitive and diffusion components, with a primary emphasis on surface contributions following carbonization. The results demonstrate that carbon composites produced from MOF–COF are effective electrode materials for supercapacitors.

Received 16th April 2026
Accepted 24th May 2026

DOI: 10.1039/d6ra03271k

rsc.li/rsc-advances

Introduction

The high growth of the global population and the expansion of the world economy have heightened the need for energy.[1,2] Consequently, there is a high demand for effective and sustainable energy storage solutions to meet growing energy demand, reduce energy losses, and integrate advanced technologies.[3,4] In the contemporary age of rapid industrial and scientific progress, the widespread use of portable electronic devices.[5,6] Among several energy storage technologies, supercapacitors offer high power density and long cycle life.[7,8] The performance depends on the structural and compositional properties of their electrode.[9,10] Thanks to advances in materials, supercapacitors have seen substantial improvements, particularly in power density.[11,12] Nevertheless, their energy density is still low relative to batteries and other traditional energy storage technologies, thereby constraining their broader practical applicability.[13–15] As a result, considerable research has focused on creating supercapacitors by exploring the performance of new materials.[16] These materials offer advantages, including superior electrical conductivity and exceptional cycle stability. The low availability of active surface sites and the existence of inactive volume in these electrodes limit their specific capacitance. This constraint restricts their overall efficacy and practical utility. Conventional electrode materials, *e.g.*, carbon materials,[17,18] metal oxides,[19,20] layered double hydroxides,[21] pervoskites,[22] ceramics,[23] metal chalcogenides,[24] and conductive polymers,[25–28] have significantly advanced supercapacitor technology. Nonetheless, their widespread commercial use is frequently hindered by several problems, including energy-intensive synthesis methods and limited stability. To mitigate these limitations, researchers have focused on developing improved electrode materials, including hybrid materials.[29–31] These hybrid systems integrate the benefits of multiple material components, thereby facilitating superior electrical conductivity, enhanced redox activity, and more effective charge-transport pathways.[32,33] Consequently, hybrid materials have been considered a promising electroactive component for markedly improving the electrochemical performance of next-generation supercapacitors.

Metal–organic frameworks (MOFs) are hybrid porous materials.[34–37] They offer high specific surface area, homogeneous and adjustable pore diameters, well-defined morphologies, and surfaces amenable to chemical modification with functional organic linkers. These features have made MOFs highly regarded for several applications, establishing them as promising materials for enhanced supercapacitors.[38,39] MOFs can be used as precursors for the production of flexible electrode materials.[40] They can produce various functional nanostructures, including MOF-derived porous carbon/metal oxides with regulated morphologies, such as yolk–shell spheres[41] and

---

[a] *Department of Chemistry, College of Science, Imam Mohammad Ibn Saud Islamic University (IMSIU), Riyadh, 11623, Saudi Arabia. E-mail: hnabdelhamid@imamu.edu.sa*

[b] *Chemistry Department, Faculty of Science, New Valley University, El-Kharja, Egypt. E-mail: mervatibrahim1990@sci.nvu.edu.eg*

metal phosphides,[42] by heat or chemical transformation. These structures can be integrated into carbon matrices or heteroatom-doped carbon nanomaterials to create highly porous frameworks with enhanced shape and electrochemical performance.[43–45] MOF@MOF-generated Co_2P/Ni_2P have been reported for supercapacitors.[46] Metal oxides were produced using MOF derivatization, including ZnO,[47] CuO,[48] Fe_2O_3,[49,50] ZnSe/CoSe,[51] Co_2P/Ni_2P,[46] and $Cu(Co–Ni)_2S_4$ nanotubes.[52] Furthermore, MOFs enable one-step synthesis of bimetallic oxides *via* carbonization of bimetallic MOF precursors, thereby creating materials with dual or multifunctional characteristics for various energy applications.[53–55] Materials produced from MOFs have facilitated the advancement of micro-supercapacitors.[56–58] Zirconium-based MOFs (Zr-MOFs) are of interest because of their exceptional chemical and thermal stability, arising from robust coordination bonds. Zr-MOFs exhibit exceptional stability under aqueous conditions and can be further modified for various applications. They exhibit large surface area and well-regulated architectures, promoting superior ion diffusion and higher capacitance, thereby enhancing charge storage capacity.[59] Notwithstanding these properties, other challenges present, including structural deterioration during cycling, intricate production procedures, and limited long-term electrochemical stability.[60] To address these limitations, UiO-66-based supercapacitors have been enhanced by conjugation with materials, such as MoS_2,[61] and polymers.[62,63] The integration of MOFs with advanced materials such as MXenes has enabled the fabrication of Ni-MOF microbelts for supercapacitors,[64] while MOF composites combined with graphene oxide[65] have been proposed as effective smart supercapacitor systems owing to their improved conductivity, structural stability, and electrochemical activity.

Covalent-organic frameworks (COFs) exhibited unique structural features, high surface area, tunable porosity, and ordered frameworks, as well as promising electrochemical performance.[66–68] These characteristics make COFs attractive for supercapacitors. For example, COFs have been employed as negative electrode materials in supercapacitors.[69] In addition, their well-defined porous structures and lightweight frameworks enable the fabrication of flexible electrodes for advanced energy storage devices.[70,71] The material performance depends on several parameters, including the pore shape and the compact arrangement of counterions within smaller pores.[72] Despite these advantages, pristine COF materials generally exhibit limited specific capacitance due to their relatively low electrical conductivity. To overcome this limitation, COFs have been integrated with other functional materials, such as carbon nanomaterials,[73] metals/ionic liquids,[74] and MXene-based structures.[75] These hybrid systems enhance electrical conductivity, provide additional active sites, and improve overall electrochemical performance. Therefore, further exploration and integration of COFs with advanced materials could lead to significant improvements in their electrochemical properties and broaden their applications in high-performance energy storage systems.

A composite material comprising MOF and COF was synthesized and characterized for potential supercapacitor applications. A melamine-based COF was integrated with the UiO-66 MOF and used as a precursor for subsequent carbonization. The structural and morphological properties of the materials were analyzed using X-ray diffraction (XRD), X-ray photoelectron spectroscopy (XPS), electron microscopy (transmission (TEM) or scanning (SEM)), Fourier transform infrared spectroscopy (FT-IR), and thermogravimetric analysis (TGA). The resulting materials were further investigated using cyclic voltammetry (CV) and galvanostatic charge/discharge (GDC) in supercapacitor applications.

Experimental

Materials and methods

Melamine and terephthalaldehyde were obtained from Merck (USA) and Fluka (Germany), respectively. Dimethyl sulfoxide (DMSO) was obtained from Fisher BioReagents. Dimethylformamide (DMF), acetic acid (AcOH), 1,4-benzenedicarboxylic acid (BDC), polyvinylidene fluoride (PVDF), and $ZrOCl_2$ were obtained from Sigma Aldrich (Germany).

Preparation of COF

The COF material was synthesized by dissolving 313 mg of melamine and 250 mg terephthalaldehyde in DMSO (15.5 mL). The resulting mixture was heated at 180 °C for 72 h to facilitate COF formation, following a previously reported method.[76,77] The product was separated *via* filtration and subsequently washed with acetone and THF. Finally, the obtained material was dried under vacuum at 120 °C to yield the purified COF product.

Synthesis of UiO-66

The solvothermal method was used to synthesize UiO-66.[78,79] Equal amounts (750 mg) of $ZrOCl_2$ and BDC were dissolved *via* ultrasonication (30 min) in a solvent mixture of acetic acid (AcOH, 4 mL) and DMF (90 mL). The mixture was heated at 120 °C for 24 h. After the reaction, the solid product was collected and rinsed with DMF (3 × 30 mL) and ethanol (3 × 30 mL) to remove residual solvents and unreacted precursors. Finally, the sample was dried in an oven overnight at 85 °C.

Synthesis of UiO-66@COF and their carbonization

The UiO-66@COF was prepared by dispersing equal amounts of UiO-66 and COF (0.2 g each) in ethanol (50 mL) and stirring continuously for 12 h to ensure uniform mixing and interaction between the two components. The product was separated by filtration and washed using water (3 × 30 mL) and ethanol (3 × 30 mL) to remove residual impurities. The obtained filtrate was then dried under vacuum at 85 °C overnight to yield the UiO-66@COF.

Subsequently, the carbonization of the UiO-66@COF composite was carried out under ambient conditions at 400 °C, 500 °C, and 700 °C. The resulting carbonized materials were denoted as UiO66@COF_400, UiO66@COF_500, and UiO66@COF_700, respectively. These carbonized composites were further investigated for their structural and electrochemical properties.

Characterization

The morphology was evaluated using TEM (JEOL 2100F) and SEM (Quattro S, Thermo Scientific) images. The crystalline phase and structural properties of the material were analyzed by powder XRD using a Phillips PW1700 diffractometer (Cu Kα, 1.5 Å). FT-IR spectroscopy was performed on a Nicolet spectrophotometer (model 6700). TGA was measured using a TA-60 thermal analyzer (Shimadzu, Japan). XPS analysis was performed using Alpha-K (Thermo Fischer, USA).

Electrochemical measurements

The working electrode was prepared by mixing the materials with carbon black and PVDF (80 : 10 : 10 (weight percentage)), then grinding the mixture in a mortar to obtain a homogeneous powder, and dispersing it in DMF to form a uniform slurry. The slurry was spread onto a nickel foam ($1 \times 1.5\ \text{cm}^2$) and subsequently dried in an oven at 80 °C overnight to ensure proper adhesion and solvent removal. An Hg/HgO electrode and a platinum mesh or graphite electrode were used as the reference and counter electrodes, respectively in an electrolyte of KOH (6 M). The measurements were evaluated using a Corrtest® 150M (Wuhan, China). The capacity (C/g) was calculated using the following equation (eqn (1)):-

$$Q = \frac{\int I \mathrm{d}V}{2 \times m \times v} \tag{1}$$

The charge-storage mechanism of the supercapacitor electrodes was further analyzed using CV data *via* the *b*-value and Dunn's methods. The *b*-value was determined using (eqn (2)):

$$\text{Current } (i) = av^b \tag{2}$$

Dunn's method was applied using eqn (3):

$$i(V) = k_1 v + k_2 v^{1/2} \tag{3}$$

where $k_1 v$ refers to the capacitive contribution, and $k_2 v^{1/2}$ represents the diffusion-controlled contribution.

The Trasatti method can be expressed in terms of the total charge (Q_{total}) and outer-surface charge (Q_{outer}) to distinguish between surface-accessible and diffusion-controlled charge storage in supercapacitor electrodes (eqn (4)). The total stored charge is composed of two contributions:

$$Q_{\text{total}} = Q_{\text{outer}} + Q_{\text{inner}} \tag{4}$$

where: Q_{total} = total charge stored at low scan rate, Q_{outer} = charge associated with the easily accessible outer surface, and Q_{inner} = diffusion-controlled inner charge originating from pores or bulk active sites. Q_{total} and Q_{outer} were determined using eqn (5) and (6):

$$\frac{1}{Q} = \frac{1}{Q_{\text{total}}} + k_1 v^{1/2} \tag{5}$$

$$Q = Q_{\text{outer}} + k_2 v^{-1/2} \tag{6}$$

Results and discussion

Materials characterization

Fig. 1 describes the synthesis procedures for UiO-66, COF, and UiO-66@COF, as well as their carbonization. The COF was prepared *via* condensation of melamine and terephthalaldehyde in an organic solvent under solvothermal conditions. The reaction product was separated, thoroughly washed with organic solvents to remove impurities and unreacted

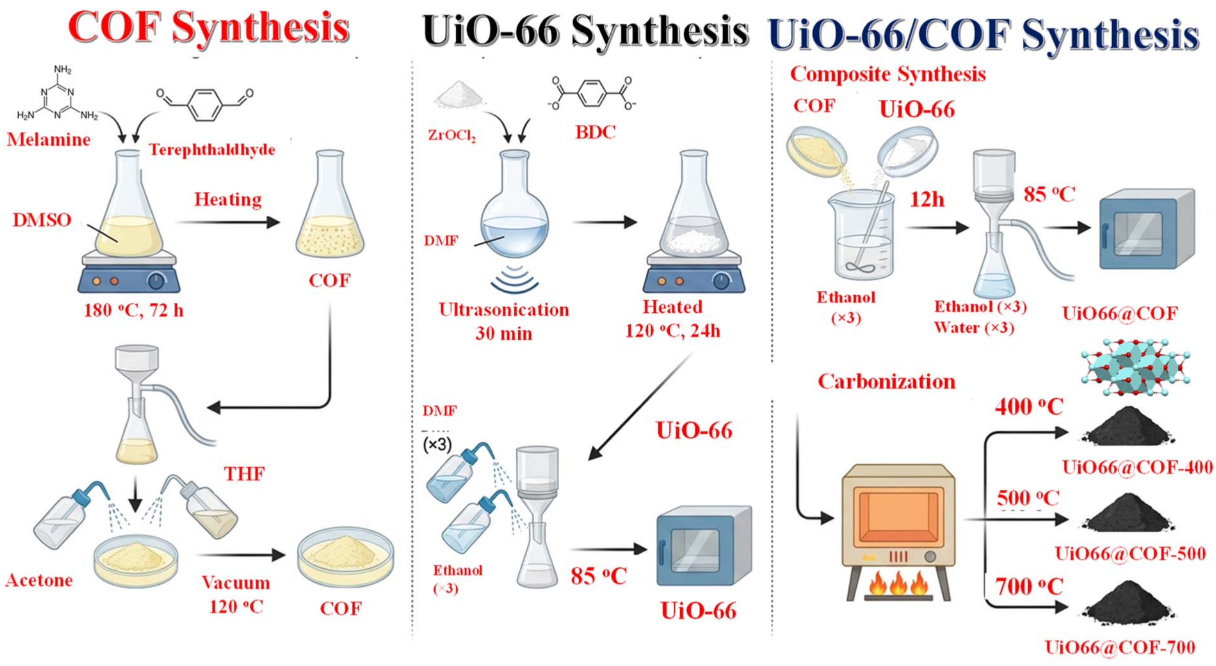

Fig. 1 Schematic representation of the materials synthesis.

precursors, and dried under vacuum to obtain the pure COF material (Fig. 1). The zirconium-based MOF, UiO-66, was synthesized *via* a solvothermal technique, in which a zirconium precursor and an organic linker were dissolved in an organic solvent with the addition of a modulating agent. The homogeneous solution was placed in an autoclave and heated to promote crystallization of the framework. The resultant product was subsequently collected, thoroughly washed with suitable solvents to eliminate residual reactants, and dried to get the final UiO-66 material (Fig. 1). The UiO-66@COF composite was prepared by dispersing the two components in a solvent and agitating the mixture for an extended period to ensure optimal interaction and uniform distribution. The composite material was then collected *via* filtration, rinsed to remove weakly bound entities, and dried under vacuum. The resultant composite was subjected to thermal treatment at various temperatures to produce carbonized materials. The framework acted as a precursor to produce zirconia particles embedded in nitrogen-doped carbon, yielding hybrid materials appropriate for electrochemical applications (Fig. 1). The materials were characterized using XRD (Fig. 2a and b), TGA (Fig. 2c), XRD for carbonized materials (Fig. 2d), FT-IR (Fig. 3a and b), XPS analysis (Fig. 4), SEM images (Fig. 5a–d), and TEM images (Fig. 6).

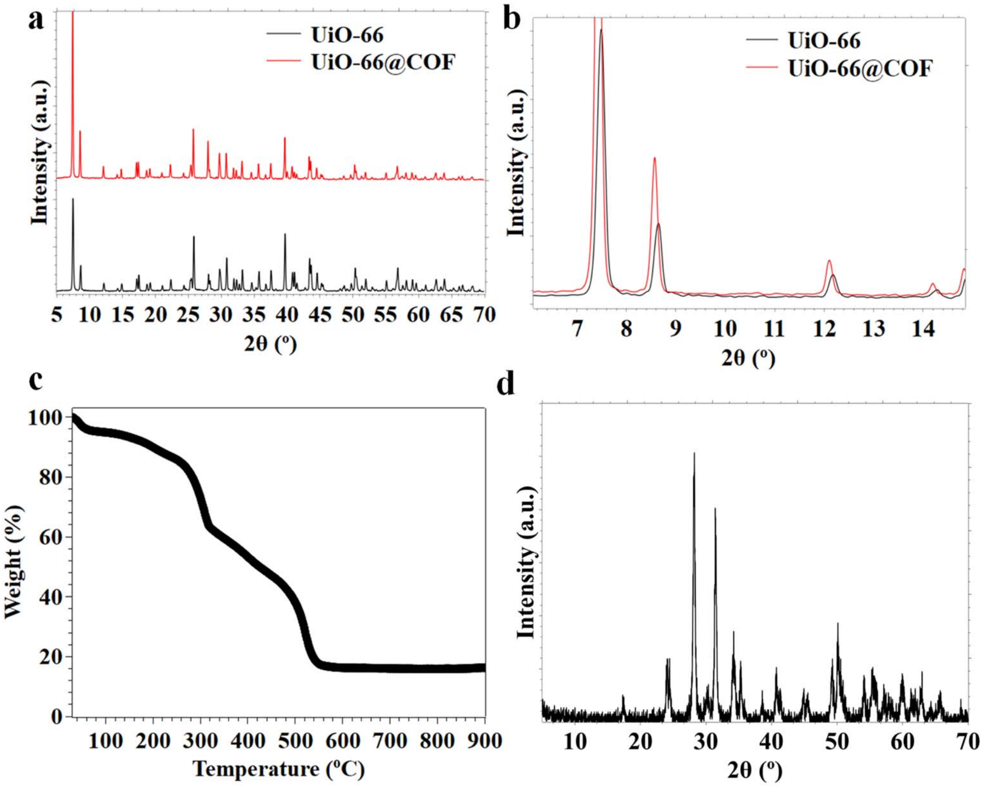

Fig. 2 (a and b) XRD for the material before carbonization, (c) TGA, and (d) XRD for UiO-66@COF_700.

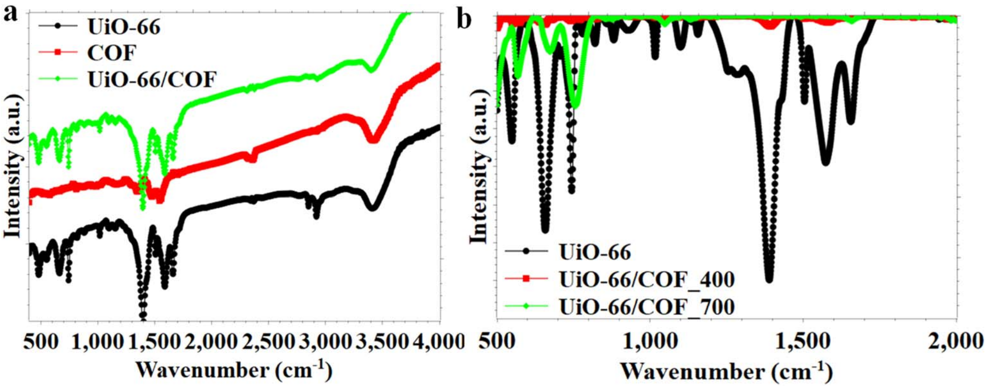

Fig. 3 FT-IR spectra for the materials (a) before and (b) after carbonization.

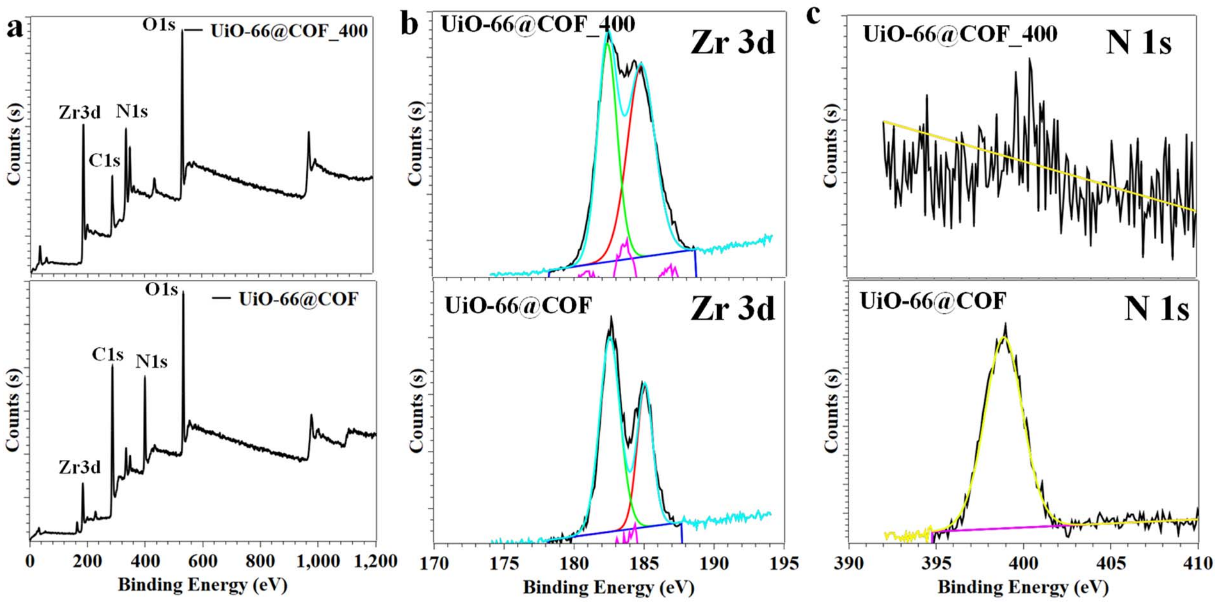

Fig. 4 XPS analysis for UiO-66@COF before and after carbonization using (a) survey, (b) Zr 3d, and (c) N 1s.

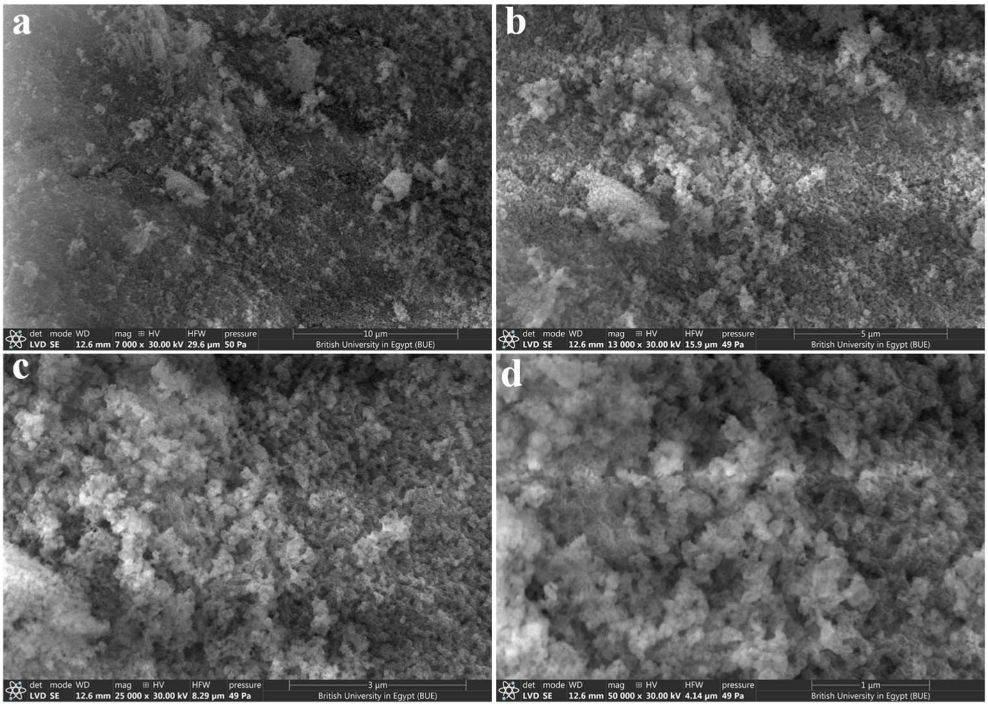

Fig. 5 SEM images for (a and b) UiO-66@COF_400 and (c and d) UiO-66@COF_700.

The crystal structure of the produced materials were evaluated *via* XRD, as seen in Fig. 2a and b. The XRD pattern of UiO-66 shows sharp diffraction peaks, indicating high crystallinity. The diffraction pattern generally exhibits pronounced Bragg reflections at low diffraction angles, indicative of the UiO-66 crystal structure. The primary diffraction peaks appear at approximately $2\theta = 7.4°$, 8.5°, 12.1°, 14.9°, and 17.2°, corresponding to the (111), (200), (220), (222), and (400) planes, respectively. The (111) peak at approximately 7.4° is the most pronounced among these reflections and is regarded as the defining peak of the UiO-66 framework. The presence of these reflections confirms the synthesis of the crystalline UiO-66 structure, characterized by a typical lattice spacing of around 20.7 Å. The XRD pattern of COF exhibits semi-crystalline properties of the prepared COF (Fig. S1).[76]

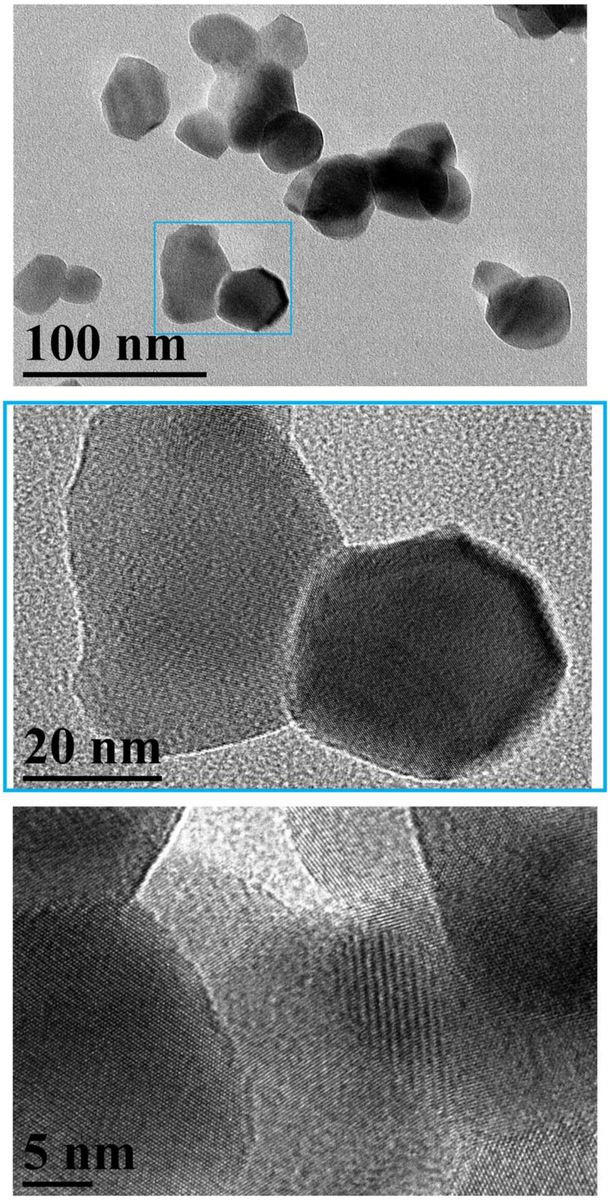

Fig. 6 TEM images and HR-TEM image for UiO-66@COF_700.

The XRD pattern of the UiO-66@COF exhibits peaks similar to those of pristine UiO-66, signifying that the crystalline structure of the MOF is maintained following its integration with the COF material. A small deviation of approximately 0.11° in the diffraction peaks is observed in the composite material (Fig. 2b). This shift indicates strong interactions between the COF and UiO-66 crystals, potentially altering the MOF's lattice environment without compromising its structural integrity. The diffraction peaks substantiate that the composite retains high crystallinity. Variations in peak intensity or minor broadening may occur due to structural flaws, such as absent linkers or clusters within the UiO-66 framework, which are prevalent in this material type.

The thermal stability and composition of the UiO-66@COF were evaluated using TGA, as illustrated in Fig. 2c. The TGA curve indicates several stages of weight loss associated with distinct heat processes. The initial weight loss of roughly 5% occurs at around 60 °C and is attributed to the removal of volatile liquids or physically adsorbed gases confined within the porous matrix. The subsequent weight loss of approximately 10% in the 60–265 °C range is attributed to the elimination of physically adsorbed water and residual organic solvents. A further weight loss of approx. 20% occurring between 265 °C and 325 °C is attributed to the thermal degradation of the COF component. Subsequently, another weight loss of about 20% occurs in the temperature range of 325–480 °C, corresponding to the decomposition of the UiO-66 framework. The mass losses of the COF and MOF components suggest that the composite comprises almost equal amounts of COF and UiO-66, aligning with the 1 : 1 ratio employed in the synthesis. Upon complete disintegration, approx. 16% of residual mass remains, corresponding to the creation of zirconium dioxide (ZrO_2) from the zirconium nodes of UiO-66. The remaining amount aligns closely with the theoretical yield of ZrO_2 anticipated from the decomposition of the MOF structure.

Carbonization tests were conducted at various temperatures to transform the composite into zirconia embedded in nitrogen-doped carbon (ZrO_2@N-doped carbon), as indicated by the TGA data. The composite precursor underwent thermal treatment at 400 °C, 500 °C, and 700 °C, yielding materials designated as UiO-66@COF_400, UiO-66@COF_500, and UiO-66@COF_700, respectively. Fig. 2d displays the XRD pattern of the carbonized material UiO-66@COF_700. The diffraction pattern exhibits distinct peaks at 2θ values of approximately 17.2°, 24.1°, 28.2°, 31.4°, 34.2°, 35.4°, 40.7°, 50.4°, and 60.0°, corresponding to the (−111), (111), (120), (022), and (131) crystallographic planes of monoclinic ZrO_2. These observations align well with the standard diffraction data for monoclinic zirconia (ICDD File no. 37-1484), validating the conversion of the MOF structure into crystalline ZrO_2 after carbonization.

FT-IR spectroscopy was investigated to examine the chemical structure of the materials both before and after carbonization (Fig. 3). The FT-IR spectra of UiO-66 exhibit distinct absorption bands at approximately 3400 cm^{-1}, 2920 cm^{-1}, and 2860 cm^{-1}, which are indicative of O–H and C–H stretching vibrations (Fig. 3a). The bands at 1598 cm^{-1} (asymmetric) and 1398 cm^{-1} (symmetric) refer to carboxylate groups after coordination. Peaks identified at 750 cm^{-1}, 660 cm^{-1}, and 475 cm^{-1} correspond to Zr–O vibrations inside the framework. Conversely, the COF material displays distinct bands at around 1550 cm^{-1}, 1475 cm^{-1}, and 1340 cm^{-1}, which correspond to C═N and C–N, and aromatic ring vibrations. The FT-IR spectrum of the UiO-66@COF composite exhibits the bands of UiO-66, reflecting the structural attributes of the MOF component. Following carbonization (Fig. 3b), the FT-IR spectra exhibit distinct bands at approximately 750 cm^{-1}, 670 cm^{-1}, and 560 cm^{-1}, corresponding to the vibrations of ZrO_2. The absence of original UiO-66 bands indicates that the MOF framework has disintegrated during carbonization, resulting in the formation of ZrO_2 within a nitrogen-doped carbon matrix.

The elemental composition and surface chemical states of the synthesized materials were analyzed using XPS, as illustrated in Fig. 4, which includes the survey spectrum (Fig. 4a), Zr core-level spectrum (Fig. 4b), and N 1s spectrum (Fig. 4c). The XPS scan spectrum of UiO-66@COF validated the presence of O, C, N, Zr, and S elements, signifying the integration of the framework components. The O 1s spectrum was observed within the binding energy range of 527.08–538.08 eV, with a characteristic peak at 532.84 eV, corresponding to an atomic concentration of 20.1%. The C 1s signal, detected between 280.08 and 293.08 eV, with a prominent peak at 286.85 eV, exhibited the highest atomic percentage (57.94%), confirming the carbon-rich composition of the hybrid framework. The N 1s peak was observed at 399.77 eV, within the range of 391.08–405.08 eV, accounting for 18.03% of the elemental composition and ascribed to nitrogen-based COF. The Zr 3p3 peak at 334.12 eV (ranging from 328.08 to 340.08 eV) with an atomic percentage of 2.16% confirmed the existence of zirconium nodes derived from the UiO-66 framework. A weak signal of S 2p signal centered at 164.3 eV (ranging from 160.08 to 169.08 eV) with an atomic contribution of 1.77%, this element comes from dimethyl sulfoxide (DMSO) that was used during COF synthesis.[76,77]

After carbonization, the XPS spectrum of UiO-66@COF_700 exhibited notable changes in elemental distribution and surface chemistry (Fig. 4). The O 1s peak, centered at 532.19 eV within the binding energy range of 525.08–539.08 eV, exhibited a high atomic concentration of 37.7%, indicating the development of oxygen-containing surface functions after heat treatment. The C 1s peak at 286.27 eV (ranging from 280.08 to 294.08 eV) accounted for 35.85% of the overall composition, indicating retention of the carbon structure post-carbonization. Zirconium species were detected *via* the Zr 3p3 peak at 334.22 eV (ranging from 325.08 to 341.08 eV) with an atomic concentration of 11.13%, alongside the Zr 3d3 peak at 183.2 eV (spanning 181 to 185 eV), which contributed an additional 2.78%, thereby confirming the preservation of zirconium-related coordination environments post-thermal treatment. Nitrogen species were identified *via* the N KL1 peak at 1108 eV (1104.68–1112.68 eV),

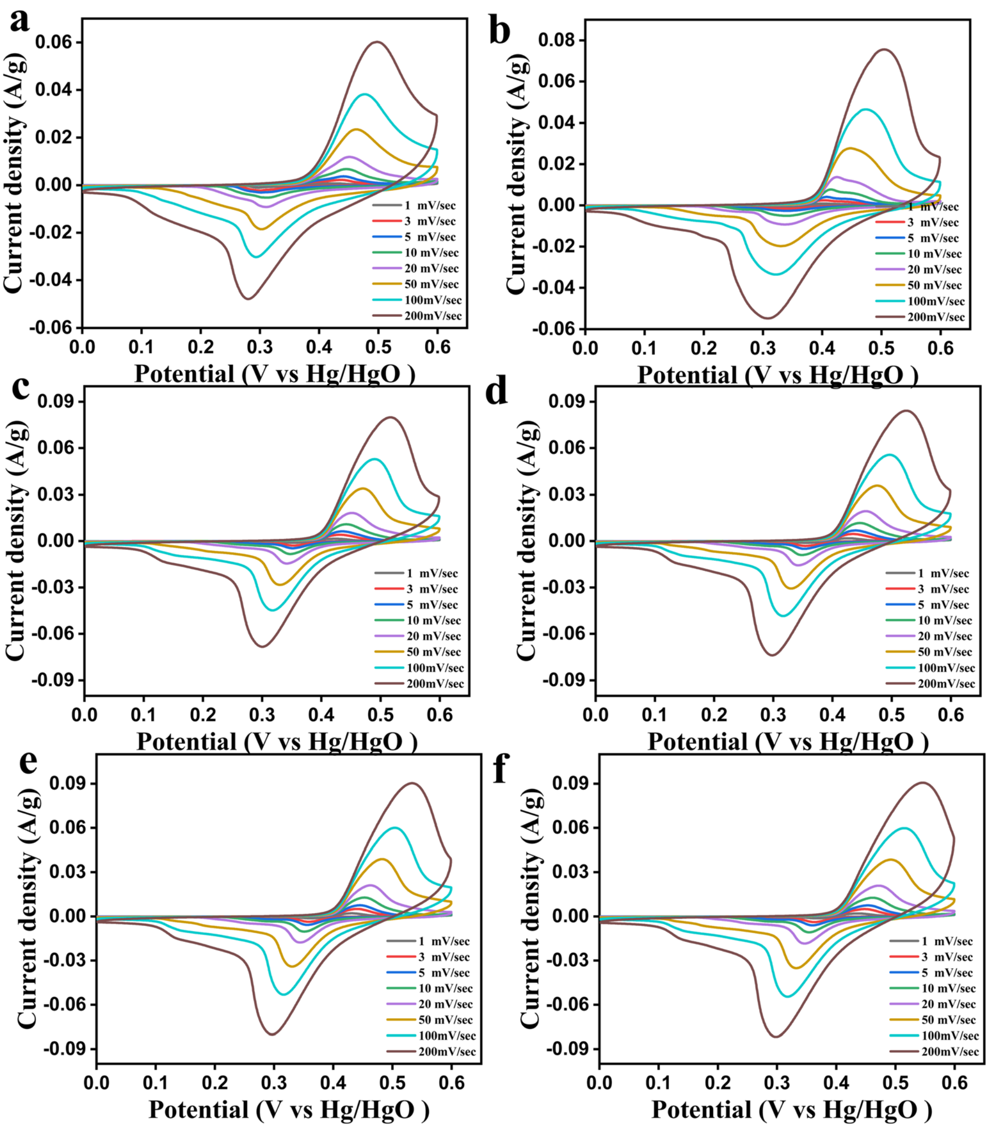

Fig. 7 CV curves for (a) UiO-66, (b) COF, (c) UiO-66@COF, (d) UiO-66@COF_400, (e) UiO-66@COF_500, and (f) UiO-66@COF_700.

contributing 9.63% at the atomic level, while a weak N 1s signal at 402.17 eV (400–404 eV) displayed a negligible atomic percentage of 0.12%. The high-resolution Zr 3d spectra displayed distinct doublet peaks at 182.5 and 185.1 eV for UiO-66@COF, which correspond to Zr $3d_{5/2}$ and Zr $3d_{3/2}$, respectively (Fig. 4b). Following carbonization, the Zr3d peaks shifted slightly to 182.5 and 184.7 eV, indicating small changes in the zirconium coordination environment due to heat treatment. The deconvoluted N 1s spectra exhibited a significant peak at 398.8 eV, typically linked to pyridinic nitrogen species, indicating effective nitrogen integration within the carbonized structure (Fig. 4c).

The morphology and particle size of the produced materials were examined *via* SEM (Fig. 5) and TEM (Fig. 6). SEM images of the carbonized materials, specifically UiO-66@COF_400 and UiO-66@COF_700 (Fig. 5a–d), demonstrate the development of nanoscale particles of around 25 to 50 nm in size. TEM images provide additional insight into the structural characteristics of the carbonized materials (Fig. 6). The TEM images clearly reveal uniformly distributed nanoparticles embedded in a carbon matrix. High-resolution TEM images show fringes with an interplanar spacing of 0.28 nm, corresponding to the monoclinic ZrO_2 planes. The heavier nanoparticles signify crystalline ZrO_2, whilst the lighter gray areas denote the remaining nitrogen-doped carbon produced during the carbonization of the COF and organic constituents of the MOF. This hybrid structure, comprising ZrO_2 nanoparticles integrated into a conductive carbon matrix, is expected to enhance the material's electrochemical performance.

Electrochemical application

The electrochemical performance of the synthesized materials was examined by CV, *b*-value analysis, Dunn's method, and GCDC tests. These investigations yield critical insights into the charge storage mechanism, electrochemical kinetics, and capacitive characteristics of the electrode materials.

Fig. 7 displays the CV curves of UiO-66, COF, UiO-66@COF, and the carbonized composites (UiO-66@COF_400, UiO-66@COF_500, and UiO-66@COF_700). The curves exhibit quasi-rectangular shapes with discernible redox peaks, indicating the presence of electric double-layer capacitance (EDLC) and pseudocapacitive characteristics. The UiO-66@COF composite exhibits a pair of distinct redox peaks at 0.51 V and 0.30 V. The peaks indicate the occurrence of reversible faradaic

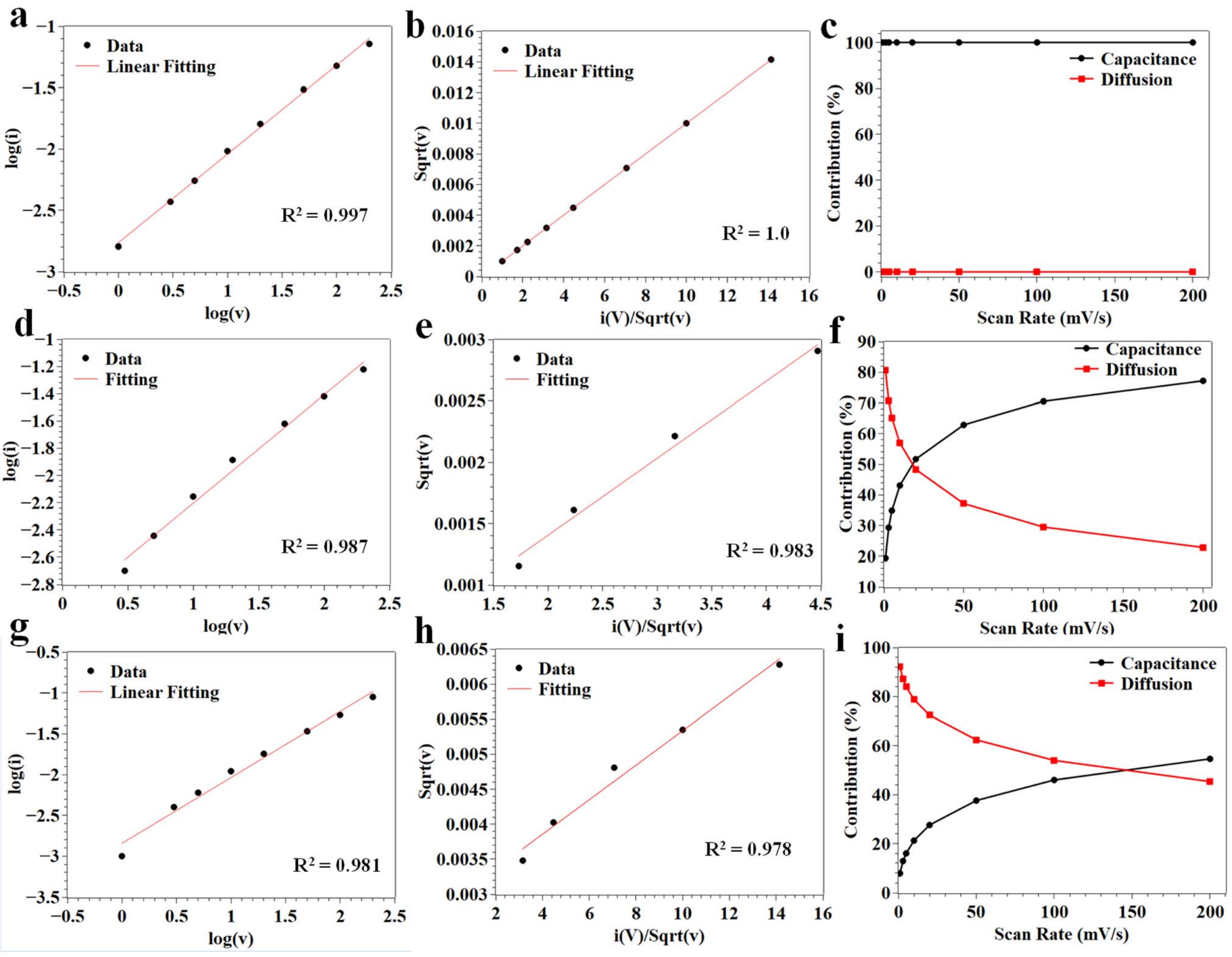

Fig. 8 *b*-value plot and Dunn method, and capacitative/diffusion contribution for (a–c) UiO-66, (d–f) COF, and (g–i) UiO-66@COF.

reactions at the electrode surface, linked to electroactive functional groups and metal centers within the composite structure. The presence of these redox peaks verifies that the charge storage mechanism includes pseudocapacitive processes and electrostatic charge accumulation. Compared with UiO-66 and COF materials, the UiO-66@COF composite and its carbonized derivatives exhibit larger enclosed CV areas, indicating improved charge storage capacity (Fig. 7). The enhancement is due to the synergistic interaction between the MOF and COF structures, as well as to the increased conductivity following carbonization. The carbonized materials, especially UiO-66@COF_700, exhibit enhanced electrochemical responses owing to the presence of zirconium dioxide nanoparticles integrated within a nitrogen-doped carbon matrix, thereby enhancing electrical conductivity and increasing the number of electroactive sites.

To enhance comprehension of charge storage kinetics, the correlation between peak current and scan rate was included (Fig. 8 and 9). The *b*-value derived from this investigation elucidates the predominant charge-storage mechanism. A *b*-value near 1 signifies a surface-controlled capacitive mechanism. The computed b-values indicate that COF is roughly 0.72, UiO-66 is about 0.80, and UiO-66@COF exhibits a high value of around 0.81 (Fig. 10a). The carbonized materials exhibit *b*-values of around 0.69, 0.75, and 0.76 for UiO-66@COF_400, UiO-66@COF_500, and UiO-66@COF_700, respectively (Fig. 10a). These data demonstrate that all materials exhibit hybrid capacitive and diffusion-controlled processes. The high *b*-value noted for the UiO-66@COF composite implies that the conjunction of MOF and COF improves surface-controlled electrochemical reactions, whereas the reduced values for the carbonized samples suggest that ion diffusion within the porous carbon matrix also plays a crucial role in the overall charge storage mechanism.

Dunn's approach was then used to determine the capacitive and diffusion contributions to the total current (Fig. 10b). COF exhibits predominantly capacitive behavior, with almost 99.99% of the current arising from surface-controlled mechanisms and a small contribution from diffusion. Conversely, UiO-66 exhibits primarily diffusion-controlled characteristics, with approximately 81% of the charge storage attributed to ion diffusion within the porous framework and only 19% to

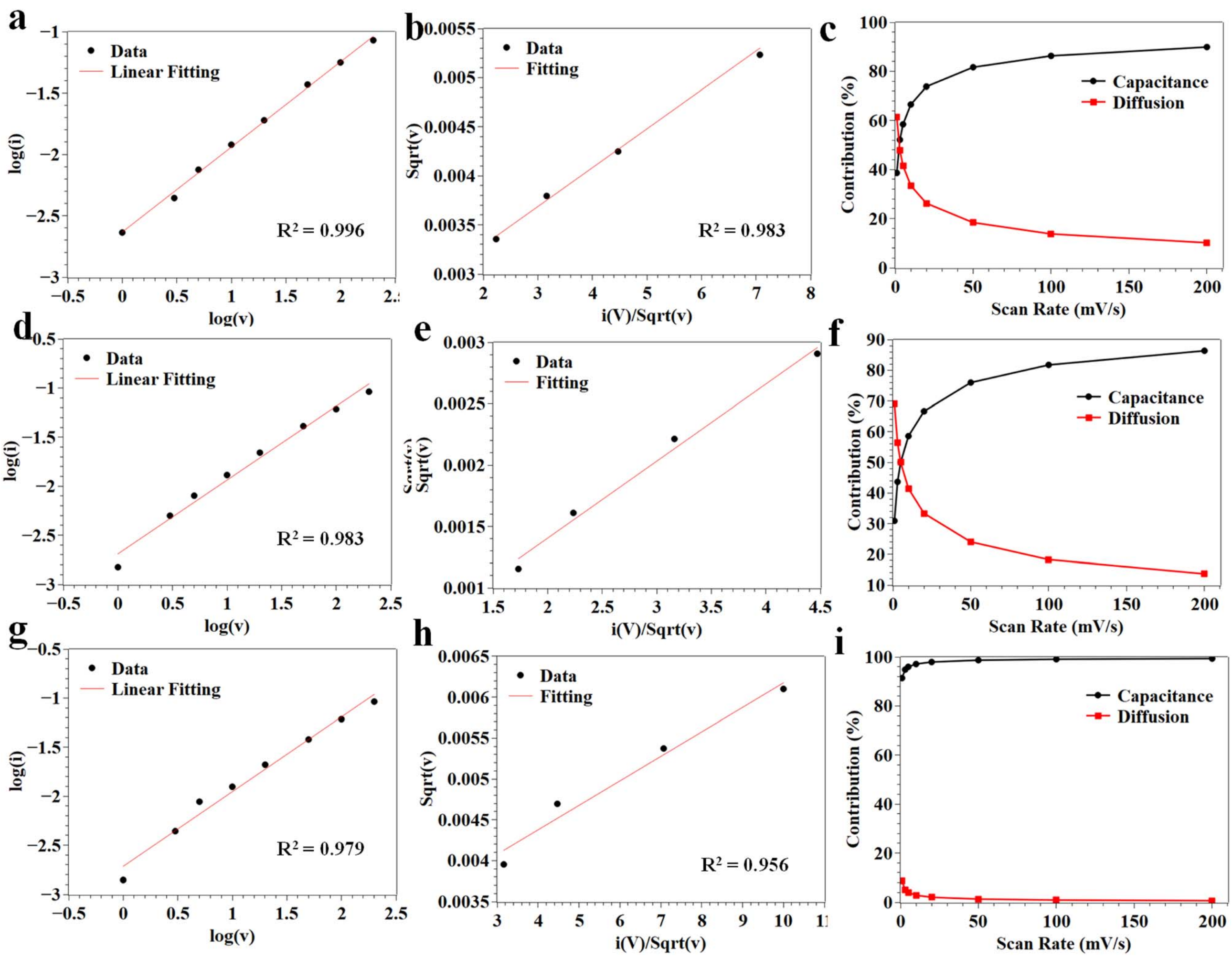

Fig. 9 *b*-value plot and Dunn method, and capacitative/diffusion contribution for (a–c) UiO-66@COF_400, (d–f) UiO-66@COF_500, (g–i) UiO-66@COF_700.

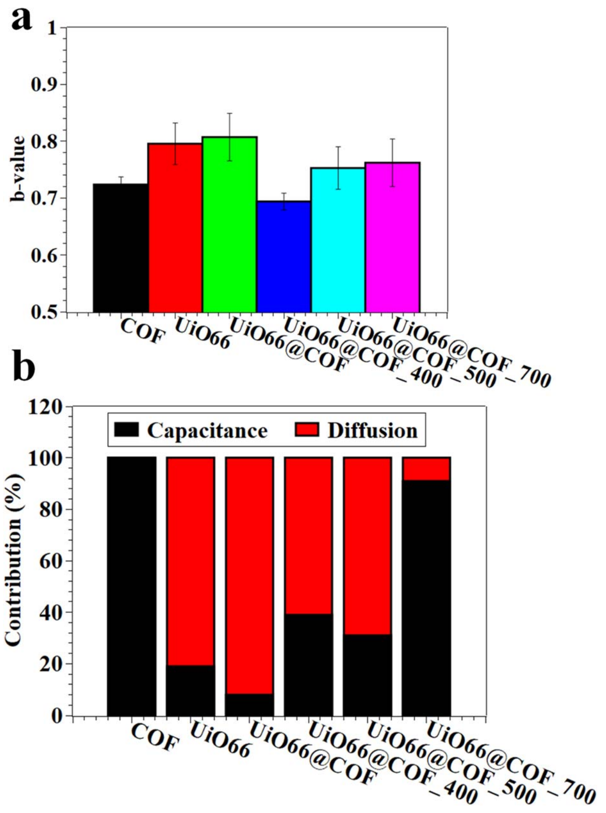

Fig. 10 (a) *b*-values for different materials and (b) capacitative/diffusion contribution for different materials.

capacitive mechanisms. The UiO-66@COF composite exhibits a substantial diffusion-controlled contribution of around 92%, indicating that ion transport within the linked porous framework is pivotal to the charge storage process. The charge storage mechanism undergoes a significant transformation post-carbonization. UiO-66@COF_400 demonstrates roughly 39% capacitive contribution and 61% diffusion contribution, whereas UiO-66@COF_500 displays about 31% capacitive contribution and 69% diffusion contribution. Conversely, UiO-66@COF_700 exhibits a predominantly capacitive characteristic, with an estimated 91% capacitive contribution and only 9% diffusion-controlled contribution. The transition to capacitive behavior is due to the development of a conductive nitrogen-doped carbon network during carbonization, which improves electron transport and facilitates quick surface-controlled charge storage (Fig. 10b).

The Trasatti approach is frequently used in supercapacitor investigation to distinguish between surface-controlled capacitive charge storage (*i.e.*, capacitance, as shown in the Dunn method above) and diffusion-controlled contributions, based on the scan-rate dependence of capacitance derived from CV measurements (Fig. 11). At low scan rates, electrolyte ions can completely penetrate both the external surface and the internal porous structure of the electrode, yielding the total capacitance (Q_{total}). Conversely, at high scan rates, only the readily accessible outer surface contributes, corresponding to the surface capacitance. In contrast to *b*-value analysis and Dunn's method (Fig. 8–10), which assess electrochemical kinetics based on current values, the Trasatti method emphasizes ion accessibility and the distribution of capacitance within the electrode architecture (Fig. 11). As a result, these approaches may produce varying trends in porous or pseudocapacitive materials. However, we perfom the analysis to support the analysis of *b*-value and Dunn method, *vide supra*. In carbonized UiO-66@COF-derived electrodes, carbonization enhances conductivity, increases accessible active sites, and improves electrolyte penetration, resulting in high capacitive contributions from Trasatti or Dunn analysis, despite a slight decrease in the b-value due to small diffusion limitations within microporous domains. However, Fig. 11 shows a similar trend of the materials, ensuring the high capacitance (surface) contribution over diffusion contribution. These methods ensure that the materials exhibit pseudocapacitance with small contributions of EDLC.

Fig. 12 displays the GCDC curves for all materials. The curves exhibit nearly symmetric triangular shapes, indicating high electrochemical reversibility and effective charge–discharge mechanisms. The specific capacitance values were calculated at various current densities (Fig. 13a). At 1 A g^{-1}, COF demonstrates a specific capacitance of around 116 F g^{-1}, whereas UiO-66 has a slightly lower value of about 107 F g^{-1} (Fig. 13b). The UiO-66@COF composite exhibits a high capacitance of 149 F g^{-1}, indicating that the integration of MOF and COF structures improves electrochemical performance (Fig. 13b). Post-carbonization, the capacitance exhibits further enhancement, with UiO-66@COF_400, UiO-66@COF_500, and UiO-66@COF_700 demonstrating values of around 164 F g^{-1}, 180 F g^{-1}, and 195 F g^{-1}, respectively (Fig. 13b). The high capacitance of UiO-66@COF_700 is ascribed to enhanced electrical conductivity and the incorporation of ZrO_2 within a conductive nitrogen-doped carbon matrix. The specific capacitance of UiO-66@COF_700 decreased from approximately 195 F g^{-1} at 1 F g^{-1} to roughly 153 F g^{-1} at 10 F g^{-1}, around 102 F g^{-1} at 30 F g^{-1}, and about 70 F g^{-1} at 50 F g^{-1} (Fig. 13a). Notwithstanding this reduction, the material retains a comparatively high capacitance at increased current densities, indicating commendable rate capability.

The cycling of UiO-66@COF_700 was assessed across 5000 cycles at 10 A g^{-1}, as illustrated in Fig. 13c. The material exhibits exceptional cycling stability, with no loss of capacitance during cycling. The exceptional stability is due to the resilient architecture of ZrO_2 nanoparticles integrated into the nitrogen-doped carbon matrix, which inhibits structural deterioration over successive charge–discharge cycles. The results indicate that the carbonized UiO-66@COF composites exhibit markedly enhanced electrochemical performance compared with the pristine materials. Among the analyzed samples, UiO-66@COF_700 exhibits superior performance owing to its optimized conductive carbon network, improved surface-controlled charge storage characteristics, and stable hybrid structure, rendering it a suitable electrode material for a supercapacitor.

Table 1 compares the electrochemical performance of the developed material with reported MOF- and COF-based

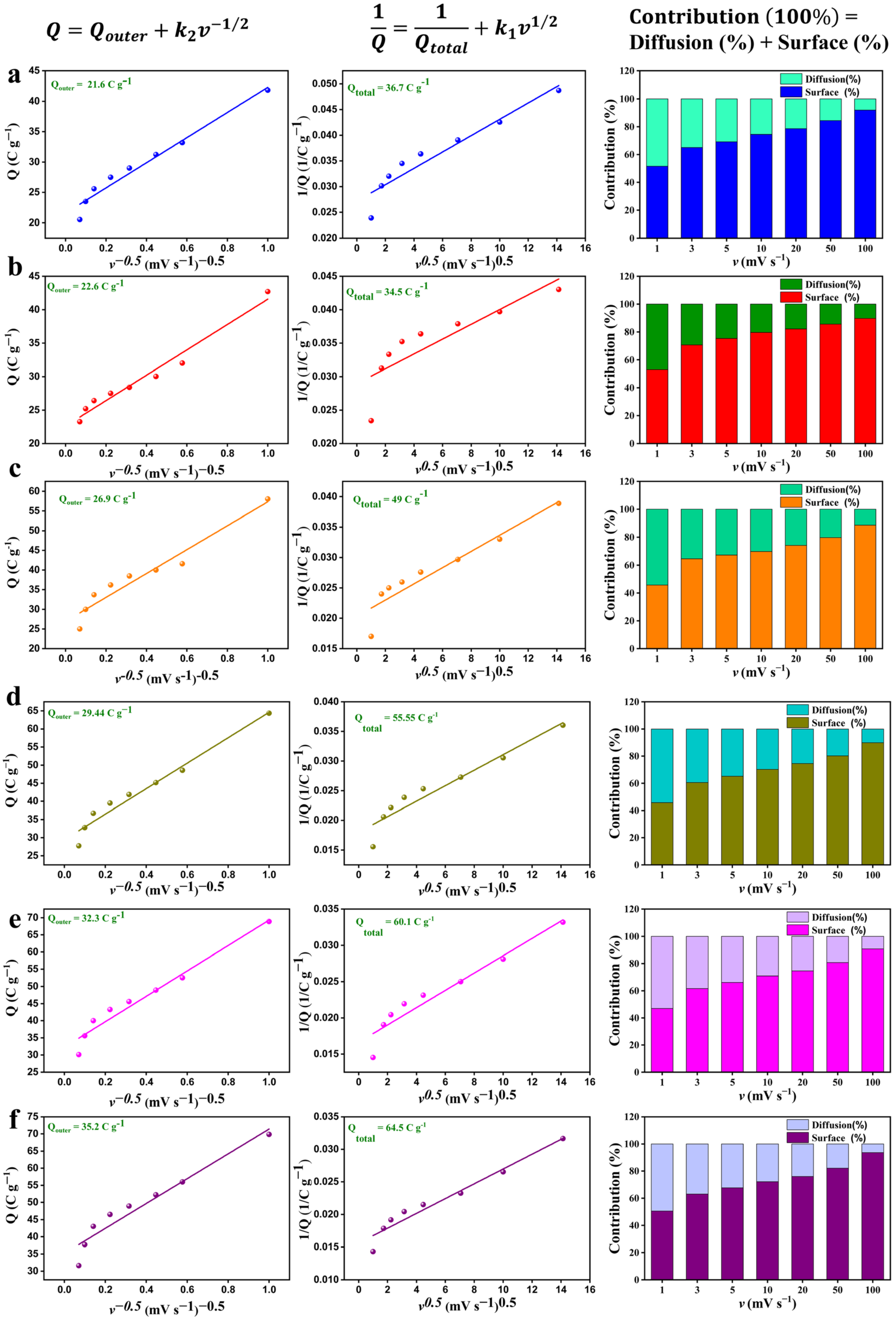

Fig. 11 Trasatti approach for (a) UiO-66, (b) COF, (c) UiO-66@COF, (d) UiO-66@COF_400, (e) UiO-66@COF_500, and (f) UiO-66@COF_700.

electrode materials.[80] Among these materials, the zirconium-based MOF UiO-66 has attracted considerable attention due to its structure composed of zirconia-based clusters and BDC organic linkers, where $Zr_6O_4(OH)_4$ oxoclusters are coordinated with twelve BDC ligands to form a highly stable framework with high thermal stability and chemical resistance arising from

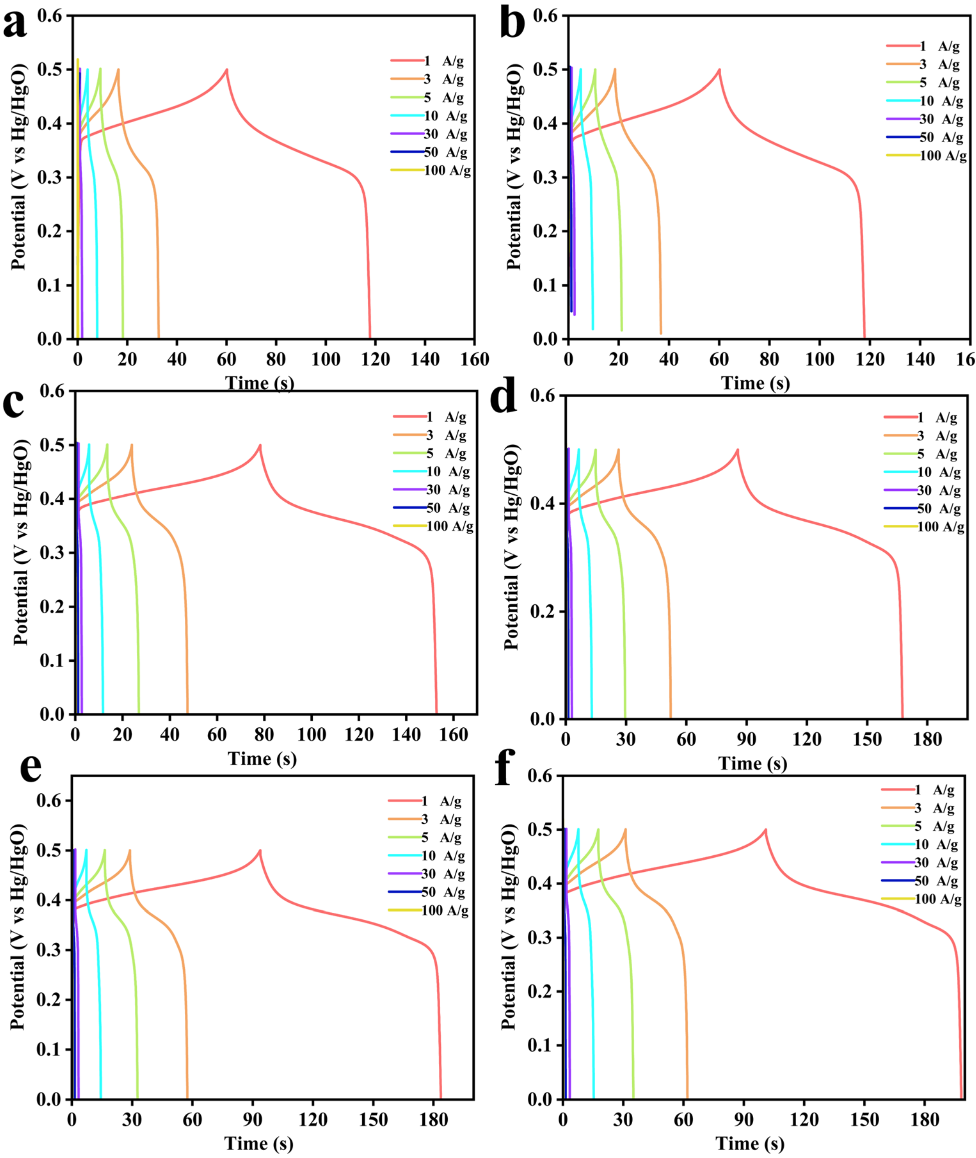

Fig. 12 GCDC for (a) UiO-66, (b) COF, (c) UiO-66@COF, (d) UiO-66@COF_400, (e) UiO-66@COF_500, and (f) UiO-66@COF_700.

strong Zr–O bonds. Previous studies have shown that synthesis conditions significantly influence the morphology, crystallinity, and conductivity of UiO-66, which directly affect its electrochemical performance; for example, controlling the pH and using acetic acid as a modulating and capping agent can tune the structure, while carbonization and acid treatment improve conductivity and create additional pores, leading to enhanced capacitance values of about 117.7 F/g and good cycling stability with approximately 84.5% capacitance retention after 7000 cycles.[63] Conductive carbon materials such as graphene oxide nanoribbons (GONRs) or functionalized carbon nanotubes (FCNTs) enhance electrical conductivity, increase surface area, and provide interconnected conductive networks, resulting in higher capacitance and cycling stability over 10 000 cycles.[81] Similarly, covalently attaching amine-functionalized UiO-66 (UiO-66-NH_2) to graphene acid produces a hybrid structure with hierarchical porosity and an interconnected conductive network, delivering a high capacitance of up to 651 F/g and maintaining 88% after 10 000 cycles.[82] MOF-derived nanoporous carbons have also been widely studied, with carbons synthesized using MOF-5 templates exhibiting high surface areas and stable capacitive behavior, with capacitance values above 100 F/g when carbonized at higher temperatures, although insufficient carbonization can result in poor conductivity and reduced capacitance despite large surface areas.[44] In addition, MOF-derived metal oxides, such as Fe_2O_3 obtained from Fe-MOF templates, exhibit promising electrochemical performance due to their tunable morphology and high surface area, delivering high capacitance and excellent cycling stability in asymmetric supercapacitors.[50] Other advanced MOF systems, including $Mn_3(HHTP)_2$ combined with ionic liquid electrolytes, have shown improved ion accessibility, reduced interfacial

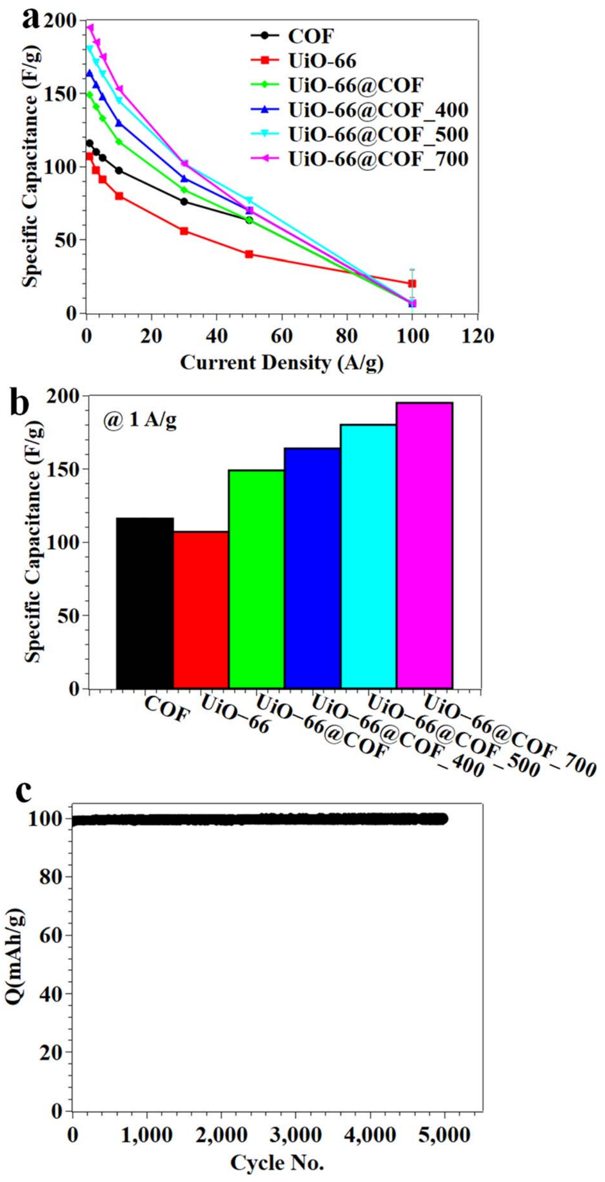

Fig. 13 Specific capacitance *versus* (a) current densities and (b) different materials, and (c) cycling for 5000 cycles at 10 A g^{-1} for UiO-66@COF_700.

resistance, and enhanced energy density with stable cycling performance.[83] Similarly, COF-based composites combined with GO provide hierarchical porosity, improved ion-transport pathways, and additional redox-active sites, thereby enabling capacitance values as high as 238.39 F/g for supercapacitor electrodes.[73] Overall, these studies demonstrate that the electrochemical performance of MOF- and COF-based materials can be significantly enhanced through strategies such as structural optimization, hybridization with conductive carbon materials, and controlled carbonization processes, which improve conductivity, increase accessible surface area, facilitate ion diffusion, and introduce additional redox-active sites for advanced energy storage applications.

Table 1 Comparison among different MOFs or COFs for supercapacitors

Materials	Synthesis methods	Conditions	Capacitance	Electrolyte	Cycling	Ref.
MOF5-derived ZnO/C	Solvothermal FA-loading Carbonization	Heating at 80 °C for 24 h Heating at 150 °C for 6 h	167 F g^{-1} at 5 mV s^{-1}	1 M H_2SO_4		44
MOF-derived Fe_2O_3	Solvothermal method Carbonization	Heated at 120 °C for 12 h 400 °C and maintained at that temperature for 2 h	96.8 mAh g^{-1} at 1 A g^{-1}	3 M KOH	90.5% after 10 000 cycles at 2 A g^{-1}	50
UiO-66	Carbonization Acid treatment	120 °C for 24 h 800 °C for 2 h HF acid treatment	117.7 F g^{-1}	1 M H_2SO_4		63
Zr-MOFs/FCNTs, or GONRs	Solvothermal	120 °C for 24 h	450 F g^{-1} at 1 A g^{-1}	1 M H_2SO_4	102% and 128% after 10 000 cycles at 10 A g^{-1}	81
GA@UiO-66-NH_2/$Ti_3C_2T_X$	Hydrothermal Solvothermal	Heated at 130 °C with a condenser under stirring for 24 h at 120 °C for 2 days	651 F g^{-1} was recorded at 2 A g^{-1}	1 M Na_2SO_4	94% after 20 000 cycles at 5 A g^{-1}	82
$Mn_3(HHTP)_2$	Hydrothermal reaction	85 °C for 24 h	4.6 F g^{-1}@52 mA g^{-1}	[EMIM][BF_4] and [EMIM][TFSI] IL	94.34% after 2000 cycles at 8 V	83
Tp-$BDMe_2$/GO	Hummers Solvothermal	Oxidation heated at 160 °C for 110 s Heating at 120 °C for 24 h	238.39 F g^{-1} at 0.2 A g^{-1}	1 M H_2SO_4	91.80% after 10 000 cycles	73
UiO-66@COF_700	Solvothermal Carbonization	180 °C for 72 h Carbonization 700 °C	195 F g^{-1} at 1 A g^{-1}	6 M KOH	100% after 5000 cycles	This study

Conclusions

This study effectively synthesized a UiO-66@COF hybrid composite and transformed it into ZrO_2-embedded N-doped carbon by controlled carbonization. The structural amalgamation of MOF and COF frameworks yields a hierarchical porous architecture rich in electroactive sites, while the carbonization procedure markedly improves electrical conductivity. The UiO-66@COF_700 sample demonstrated superior performance among the produced materials, achieving a specific capacitance of roughly 195 F/g at 1 A/g, commendable rate capability, and exceptional cycling stability over 5000 cycles. Kinetic studies indicated that the charge-storage mechanism comprises both capacitive and diffusion-controlled processes, with surface-controlled behavior prevailing post-carbonization. The enhanced electrochemical performance is due to the interaction between ZrO_2 nanoparticles and the conductive nitrogen-doped carbon matrix, which promotes rapid electron transport and efficient ion diffusion. These findings indicate that MOF–COF-derived carbon composites are promising options for supercapacitor electrodes, offering the potential to develop high-performance energy storage materials.

Conflicts of interest

The authors declare no competing interests.

Data availability

The authors declare that the data supporting the findings of this study are available within the text.

Acknowledgements

This work was supported and funded by the Deanship of Scientific Research at Imam Mohammad Ibn Saud Islamic University (IMSIU) (grant number IMSIU-DDRSP2603).

References

1 H. Majidi, M. M. Hayati, C. Breyer, B. Mohammadi-ivatloo, S. Honkapuro, H. Karjunen, P. Laaksonen and V. Sihvonen, Overview of energy modeling requirements and tools for future smart energy systems, *Renew. Sustain. Energy Rev.*, 2025, **212**, 115367, DOI: 10.1016/j.rser.2025.115367.

2 D. Virah-Sawmy and B. Sturmberg, Socio-economic and environmental impacts of renewable energy deployments: A review, *Renew. Sustain. Energy Rev.*, 2025, **207**, 114956, DOI: 10.1016/j.rser.2024.114956.

3 A. Kerschbaum, L. Trentmann, A. Hanel, S. Fendt and H. Spliethoff, Methods for analysing renewable energy potentials in energy system modelling: A review, *Renew. Sustain. Energy Rev.*, 2025, **215**, 115559, DOI: 10.1016/j.rser.2025.115559.

4 Q. Wang, Y. Li and R. Li, Integrating artificial intelligence in energy transition: A comprehensive review, *Energy Strateg. Rev.*, 2025, **57**, 101600, DOI: 10.1016/j.esr.2024.101600.

5 T. Zhang, M. Qadrdan, J. Wu, B. Couraud, M. Stringer, S. Walker, A. Hawkes, A. Allahham, D. Flynn, D. Pudjianto, P. Dodds and G. Strbac, A systematic review of modelling methods for studying the integration of hydrogen into energy systems, *Renew. Sustain. Energy Rev.*, 2025, **208**, 114964, DOI: 10.1016/j.rser.2024.114964.

6 E. Enasel and G. Dumitrascu, Storage solutions for renewable energy: A review, *Energy Nexus*, 2025, **17**, 100391, DOI: 10.1016/j.nexus.2025.100391.

7 R. K. Maurya, A. Agarwal, R. K. Gupta, S. Masiul Islam and R. Sharma, Recent technological advancement in asymmetric supercapacitors: A comprehensive review, *J. Power Sources*, 2025, **640**, 236818, DOI: 10.1016/j.jpowsour.2025.236818.

8 N. Singh, V. Singh, N. Bisht, P. Negi, A. Dhyani, R. K. Sharma and B. S. Tewari, A comprehensive review on supercapacitors: Basics to recent advancements, *J. Energy Storage*, 2025, **121**, 116498, DOI: 10.1016/j.est.2025.116498.

9 N. Parvin, D. Merum, M. Kang, S. W. Joo, J. H. Jung and T. K. Mandal, Recent advances in hybrid supercapacitors: a review of high performance materials and scalable fabrication techniques, *J. Mater. Chem. A*, 2025, **13**, 24320–24386, DOI: 10.1039/D5TA02887F.

10 C. V. V. Muralee Gopi, S. Alzahmi, V. Narayanaswamy, R. Vinodh, B. Issa and I. M. Obaidat, Supercapacitors: A promising solution for sustainable energy storage and diverse applications, *J. Energy Storage*, 2025, **114**, 115729, DOI: 10.1016/j.est.2025.115729.

11 S. A. Beknalkar, A. M. Teli, V. V. Satale, T. S. Bhat, R. U. Amate, P. J. Morankar and J. C. Shin, A critical review on piezoelectric supercapacitors: Fundamentals, recent advances, and future directions, *J. Alloys Compd.*, 2025, **1024**, 180169, DOI: 10.1016/j.jallcom.2025.180169.

12 D. Khalafallah, D. E. E. Refaay, X. Gu, A. M. A. Henaish and Q. Zhang, Multicomponent core-shell nanostructures for supercapacitors and batteries: A review, *Energy Storage Mater*, 2025, **78**, 104284, DOI: 10.1016/j.ensm.2025.104284.

13 P. Ren, G. Yang, Y. Jin, C. Peng, X. Lei, F. Yin, Z. Zhao, Y. Wang, Z. Guo, Z. Chen and F. Ren, High entropy materials as electrode materials for supercapacitors: A review, *J. Alloys Compd.*, 2025, **1024**, 180153, DOI: 10.1016/j.jallcom.2025.180153.

14 C. V. V. Muralee Gopi, S. Alzahmi, V. Narayanaswamy, K. V. G. Raghavendra, B. Issa and I. M. Obaidat, A review on electrode materials of supercapacitors used in wearable bioelectronics and implantable biomedical applications, *Mater. Horizons*, 2025, **12**, 4092–4132, DOI: 10.1039/D4MH01707B.

15 M. Libber, N. Gariya and M. Kumar, A comprehensive analysis of supercapacitors with current limitations and emerging trends in research, *J. Solid State Electrochem.*, 2025, **29**, 513–527, DOI: 10.1007/s10008-024-06107-x.

16 J. Zia and M. S. S. R. Tejaswini, Advancements in binary and ternary transition metal-based composites for high-performance supercapacitors: a comprehensive review, *RSC Adv.*, 2025, **15**, 9055–9080, DOI: 10.1039/D5RA00528K.

17 P. Chaluvachar, Y. N. Sudhakar, G. T. Mahesha, V. G. Nair, N. Desai and D. K. Pai, Emerging role of graphitic carbon nitride in advanced supercapacitors: A comprehensive review, *J. Energy Chem.*, 2025, **103**, 498–524, DOI: 10.1016/j.jechem.2024.11.075.

18 J. Wang, T. Huo, Y. Zhao, R. Lu and X. Wu, Recent advances in heteroatoms-doped porous carbon electrode materials for supercapacitors: A review, *J. Energy Storage*, 2025, **110**, 115216, DOI: 10.1016/j.est.2024.115216.

19 J. A. Goudar, T. S. N, S. Chapi, M. M. V., M. R. Saeb and M. Salami-Kalajahi, Cobalt-Based Materials in Supercapacitors and Batteries: A Review, *Adv. Energy Sustain. Res.*, 2025, **6**(2), 2400271, DOI: 10.1002/aesr.202400271.

20 I. Gomaa, K. S. Al-Namshah and H. N. Abdelhamid, Hybrid Mesoporous Mn2O3/Carbon as Electrode Materials for Supercapacitors, *J. Clust. Sci.*, 2025, **37**, 5, DOI: 10.1007/s10876-025-02961-5.

21 C. Jing, S. Tao, B. Fu, L. Yao, F. Ling, X. Hu and Y. Zhang, Layered double hydroxide-based nanomaterials for supercapacitors and batteries: Strategies and mechanisms, *Prog. Mater. Sci.*, 2025, **150**, 101410, DOI: 10.1016/j.pmatsci.2024.101410.

22 M. Habibi, H. Sohrabi and M. Reza Majidi, Towards high-performance perovskite-based supercapacitors: A review of recent research developments, *Mater. Sci. Eng. B*, 2025, **317**, 118110, DOI: 10.1016/j.mseb.2025.118110.

23 A. I. Ali, M. M. Maghawry, H. N. Abdelhamid, A. R. Wassel, D. Choi, M. Arif, G. H. Ramzy and S. A. Abdelwahab, Structural and functional tailoring of Ba0.9Ca0.1Ti0.9Zr0.1O3 ceramics with reduced graphene oxide (rGO) for energy storage applications, *J. Mater. Sci. Mater. Electron.*, 2025, **36**, 1960, DOI: 10.1007/s10854-025-16050-w.

24 S. Liu, H. Zhang, X. Peng, J. Chen, L. Kang, X. Yin, Y. Yusuke and B. Ding, Emerging Issues and Opportunities of 2D Layered Transition Metal Dichalcogenide Architectures for Supercapacitors, *ACS Nano*, 2025, **19**, 13591–13636, DOI: 10.1021/acsnano.5c01512.

25 D. Cevher and A. Cirpan, Design, strategies and recent advances in conjugated polymers for supercapacitors, *J. Energy Storage*, 2025, **109**, 115246, DOI: 10.1016/j.est.2024.115246.

26 A. A. Saddik and H. N. Abdelhamid, Conjugated tetraphenylethene-based polymers for supercapacitor, *Polymer (Guildf).*, 2024, **315**, 127778, DOI: 10.1016/j.polymer.2024.127778.

27 K. I. Aly, S. Mostafa Ebrahium, H. N. Abdelhamid, H. M. El-Bery, A. A. K. Mohammed, C.-W. Huang and M. Gamal Mohamed, Efficient synthesis of main chain thermosetting polybenzoxazine resin containing tert-butylcyclohexanone and diphenylmethane units for supercapacitor energy storage, *Eur. Polym. J.*, 2024, **221**, 113519, DOI: 10.1016/j.eurpolymj.2024.113519.

28 M. Ibrahim, Z. Wen, X. Sun and H. N. Abdelhamid, In situ polymerization of a melamine-based microsphere into 3D nickel foam for supercapacitors, *RSC Adv.*, 2024, **14**, 5566–5576, DOI: 10.1039/D3RA08489B.

29 B. C. Yallur, M. P. Rao, M. Harshitha, D. Basrur, P. H. Umesh, V. Kamat, K. D. Venu Prasad, K. N. Venugopala and R. S. Bhat, Recent Advances in Graphene-Based Metal Oxide Composites for Supercapacitors: A Comprehensive Review, *Adv. Sustain. Syst.*, 2025, **9**(8), 2500121, DOI: 10.1002/adsu.202500121.

30 M. F. Iqbal, F. Nasir, F. Shabbir, Z. U. D. Babar, M. F. Saleem, K. Ullah, N. Sun and F. Ali, Supercapacitors: An Emerging Energy Storage System, *Adv. Energy Sustain. Res.*, 2025, **6**(8), 2400412, DOI: 10.1002/aesr.202400412.

31 R. A. Alsaiari, I. Gomaa and H. N. Abdelhamid, Eco-Engineered Co$_3$O$_4$/CoO/C Nanohybrid for Supercapacitors and Efficient Water Splitting, *Arab. J. Sci. Eng.*, 2025, DOI: 10.1007/s13369-025-10606-y.

32 T. Ramachandran, R. K. Raji and I. Hussain, Emerging trends in screen-printed supercapacitors for energy storage and power devices, *Sustain. Energy Fuels*, 2025, **9**, 6116–6149, DOI: 10.1039/D5SE00536A.

33 L. Guan, L. Guo, H. Yao, J. Cai, X. Dong, R. Wang, Z. Zhai, X. Chen, X. Wei, D. Li, X. Liu, S. Ji and F. Meng, Redox Additive Electrolytes for Supercapacitors: A Mini-Review on Recent Developments and Future Directions, *Molecules*, 2025, **30**, 1764, DOI: 10.3390/molecules30081764.

34 H.-C. Zhou, J. R. Long and O. M. Yaghi, Introduction to Metal–Organic Frameworks, *Chem. Rev.*, 2012, **112**, 673–674, DOI: 10.1021/cr300014x.

35 L. Shi, K. O. Kirlikovali, Z. Chen and O. K. Farha, Metal-organic frameworks for water vapor adsorption, *Chem*, 2024, **10**, 484–503, DOI: 10.1016/j.chempr.2023.09.005.

36 H. N. Abdelhamid and A. Mathew, Cellulose-Metal Organic Frameworks (CelloMOFs) Hybrid Materials and their Multifaceted Applications: A Review, *Coord. Chem. Rev.*, 2022, **451**, 214263, DOI: 10.1016/j.ccr.2021.214263.

37 H. N. Abdelhamid, Zeolitic Imidazolate Frameworks (ZIF-8) for Biomedical Applications: A Review, *Curr. Med. Chem.*, 2021, **28**, 7023–7075, DOI: 10.2174/0929867328666210608143703.

38 S. J. Shin, J. W. Gittins, C. J. Balhatchet, A. Walsh and A. C. Forse, Metal–Organic Framework Supercapacitors: Challenges and Opportunities, *Adv. Funct. Mater.*, 2023, 2308497, DOI: 10.1002/ADFM.202308497.

39 A. U. Rehman, S. Ullah, N. A. Khan, M. S. Javed, L. Gurbanova, M. A. Ismail, A. Mohammad, S. S. A. Shah and M. A. Nazir, MOF-Based Composite Materials for Supercapacitors: Design, Performance, and Challenges, *Chem. – An Asian J.*, 2025, **20**(17), e00453, DOI: 10.1002/asia.202500453.

40 H. N. Abdelhamid and S. A. Salim, Ferric metal-organic frameworks (MOFs)-based electrospinning fibers for supercapacitors, *React. Funct. Polym.*, 2025, **217**, 106466, DOI: 10.1016/j.reactfunctpolym.2025.106466.

41 J. Wang, S. Li, N. Fu, D. Tian, Y. Zheng, F. Wang, C. Liu, X. Wang, Z. Zhou, Y. Niu, H. Liu, G. Wang, S. Mu and J. Luo, MOF-derived carbon-coated NiS/NiS2 yolk-shell spheres as a satisfactory positive electrode material for

hybrid supercapacitors, *Adv. Compos. Hybrid Mater.*, 2025, **8**, 190, DOI: 10.1007/s42114-025-01257-6.

42 B. Ji, W. Li, F. Zhang, P. Geng and C. M. Li, MOF-Derived Transition Metal Phosphides for Supercapacitors, *Small*, 2025, **21**(12), 2409273, DOI: 10.1002/smll.202409273.

43 J. Kim, C. Young, J. Lee, Y.-U. Heo, M.-S. Park, M. S. A. Hossain, Y. Yamauchi and J. H. Kim, Nanoarchitecture of MOF-derived nanoporous functional composites for hybrid supercapacitors, *J. Mater. Chem. A*, 2017, **5**, 15065–15072, DOI: 10.1039/C7TA03356G.

44 B. Liu, H. Shioyama, H. Jiang, X. Zhang and Q. Xu, Metal–organic framework (MOF) as a template for syntheses of nanoporous carbons as electrode materials for supercapacitor, *Carbon N. Y.*, 2010, **48**, 456–463, DOI: 10.1016/j.carbon.2009.09.061.

45 Y. Yan, M. Huang, Y. Wang, D. He and J. He, M-Ni-Co MOF (M=Zn, Fe, Mn) for high-performance supercapacitors by adjusting its morphology, *Heliyon*, 2024, **10**(5), e25586, DOI: 10.1016/J.HELIYON.2024.E25586.

46 H. Qu, K. Liu, Q. Li, T. Cao, G. Chen, H. Guan, C. Dong and Z. Yin, MOF-on-MOF Derived Co2P/Ni2P Heterostructures for High-Performance Supercapacitors, *J. Phys. Chem. Lett.*, 2024, **15**, 10181–10189, DOI: 10.1021/acs.jpclett.4c02521.

47 H. N. Abdelhamid, M. Ibrahim and M. Yahia, Supercapacitor Performance Using <scp>ZIF</scp> -L@ <scp>PIM</scp> -1-Derived <scp>ZnO</scp> @N-Doped Carbon Electrodes, *J. Appl. Polym. Sci.*, 2025, **142**, e57702, DOI: 10.1002/app.57702.

48 F. K. Algethami, S. A. Al Kiey and H. N. Abdelhamid, CuO Nanoparticles on Carbon from Copper-Based Metal–Organic Frameworks (MOF) for Energy Storage, *J. Inorg. Organomet. Polym. Mater.*, 2025, **36**, 2393–2405, DOI: 10.1007/s10904-025-04037-3.

49 S. A. Al Kiey, F. K. Algethami and H. N. Abdelhamid, Ferric Oxide@Carbon-Derived from Fe-MOF for Supercapacitor, *Arab. J. Sci. Eng.*, 2025, DOI: 10.1007/s13369-025-10689-7.

50 H. Song, Z. Li, Y. Li, J. Hou, J. Sun, Y. Xie, X. Zhang and X. Fan, Structure design of MOF-derived Fe2O3 for high-performance asymmetric supercapacitors, *Compos. Commun.*, 2025, **56**, 102406, DOI: 10.1016/j.coco.2025.102406.

51 Z. M. Hassan, F. M. Elantabli, S. G. Mohamed and H. N. Abdelhamid, Metal-organic frameworks (MOFs)-derived zinc selenide and cobalt selenide for asymmetric supercapacitors, *J. Energy Storage*, 2026, **141**, 119311, DOI: 10.1016/j.est.2025.119311.

52 G. Nagaraju, S. C. Sekhar, B. Ramulu and J. S. Yu, High-performance hybrid supercapacitors based on MOF-derived hollow ternary chalcogenides, *Energy Storage Mater*, 2021, **35**, 750–760, DOI: 10.1016/j.ensm.2020.12.005.

53 U. Zahid, M. R. Khawar, S. Jang, Y. Javed, N. A. Shad, D. Choi, A. Ahmad and M. D. Albaqami, Development of Bimetallic MOF with reduced bandgap for high-performance asymmetric supercapacitors, *Electrochim. Acta*, 2025, **525**, 146103, DOI: 10.1016/j.electacta.2025.146103.

54 H. N. Abdelhamid, Ni/Cu Metal-Organic Frameworks (MOFs)-derived NiO/CuO@C for Supercapacitors and Oxygen Evolution Reaction, *Surfaces and Interfaces*, 2025, **76**, 107923, DOI: 10.1016/j.surfin.2025.107923.

55 H. N. Abdelhamid, Bimetallic Metal–Organic Framework (MOF)–Derived NiO/CuO-Embedded Carbon for Supercapacitor, *Appl. Organomet. Chem.*, 2025, **39**, e70193, DOI: 10.1002/aoc.70193.

56 S. Mumtaz, M. Imran and A. M. Afzal, Photoresponsive CoNi-MOF@CoO2@WSe2 hybrid: A dual-function platform for high-performance photo-hybrid supercapacitors and zearalenone sensing, *Inorg. Chem. Commun.*, 2025, **179**, 114788, DOI: 10.1016/j.inoche.2025.114788.

57 C. Huang, W. Sun, Y. Jin, Q. Guo, D. Mücke, X. Chu, Z. Liao, N. Chandrasekhar, X. Huang, Y. Lu, G. Chen, M. Wang, J. Liu, G. Zhang, M. Yu, H. Qi, U. Kaiser, G. Xu, X. Feng and R. Dong, A General Synthesis of Nanostructured Conductive Metal–Organic Frameworks from Insulating MOF Precursors for Supercapacitors and Chemiresistive Sensors, *Angew. Chemie Int. Ed.*, 2024, **63**(3), e202313591, DOI: 10.1002/anie.202313591.

58 F. Dai, X. Wang, S. Zheng, J. Sun, Z. Huang, B. Xu, L. Fan, R. Wang, D. Sun and Z.-S. Wu, Toward high-performance and flexible all-solid-state micro-supercapacitors: MOF bulk vs. MOF nanosheets, *Chem. Eng. J.*, 2021, **413**, 127520, DOI: 10.1016/j.cej.2020.127520.

59 I. Shahid, N. H. Solangi, R. Andavar, F. Ullah, Y. Sun, U. A. Kolachi, J. Xie, X. Li and J. Pan, The design and structural evolution of MOF-derived composite and the applications for supercapacitors and (Li, Na, K, Zn) ion batteries, *Chem. Eng. J.*, 2025, **514**, 163273, DOI: 10.1016/j.cej.2025.163273.

60 A. C. Mendhe, S. Lekshmi, N. S. Barse, I. Hussain, M. Kim, S. B. Jadhav and H. Lee, Recent progress in metal chalcogenide-MXene and MOF-derived composites for supercapacitors: synthesis, challenges, and future solutions, *Prog. Mater. Sci.*, 2026, **156**, 101558, DOI: 10.1016/j.pmatsci.2025.101558.

61 B. M. Raffah, H. Hassan, M. W. Iqbal, Y. Al-Hadeethi and B. Arkook, Novel UiO-66/MoS2 hybrid materials: Dual-functionality as battery/supercapacitor electrodes and electrocatalysts for HER, *J. Energy Storage*, 2025, **106**, 114881, DOI: 10.1016/j.est.2024.114881.

62 C. Zhang, J. Tian, W. Rao, B. Guo, L. Fan, W. Xu and J. Xu, Polypyrrole@metal-organic framework (UIO-66)@cotton fabric electrodes for flexible supercapacitors, *Cellulose*, 2019, **26**, 3387–3399, DOI: 10.1007/s10570-019-02321-3.

63 Y.-S. Sung, L.-Y. Lin and H.-Y. Lin, Study of pH value effect on synthesizing UIO-66 and carbonized UIO-66 as active material for solid-state supercapacitors, *J. Taiwan Inst. Chem. Eng.*, 2020, **116**, 197–204, DOI: 10.1016/j.jtice.2020.11.018.

64 X. Zhang, S. Yang, W. Lu, D. Lei, Y. Tian, M. Guo, P. Mi, N. Qu and Y. Zhao, MXenes induced formation of Ni-MOF microbelts for high-performance supercapacitors, *J. Colloid Interface Sci.*, 2021, **592**, 95–102, DOI: 10.1016/j.jcis.2021.02.042.

65 S. Gautam, S. Rialach, S. Paul and N. Goyal, MOF/graphene oxide based composites in smart supercapacitors:

a comprehensive review on the electrochemical evaluation and material development for advanced energy storage devices, *RSC Adv.*, 2024, **14**, 14311–14339, DOI: 10.1039/D4RA01027B.

66 X. Gao, Y. Dong, S. Li, J. Zhou, L. Wang and B. Wang, MOFs and COFs for Batteries and Supercapacitors, *Electrochem. Energy Rev.*, 2020, **3**, 81–126, DOI: 10.1007/s41918-019-00055-1.

67 Z. Peng, N. Li, Y. He, X. Shi, X. Meng, M. Lu and K. Xu, Investigation of knot-linker effects on charge storage in triangular COF supercapacitors: A molecular dynamics investigation, *J. Energy Storage*, 2025, **131**, 117484, DOI: 10.1016/j.est.2025.117484.

68 M. Younis, J. W. Han, H. Yang, A. F. M. EL-Mahdy and R. H. Lee, Redox-active covalent organic frameworks for supercapacitors: A molecular-level design and integration approach, *Renew. Sustain. Energy Rev.*, 2026, **226**, 116318, DOI: 10.1016/j.rser.2025.116318.

69 S. Kandambeth, J. Jia, H. Wu, V. S. Kale, P. T. Parvatkar, J. Czaban-Jóźwiak, S. Zhou, X. Xu, Z. O. Ameur, E. Abou-Hamad, A. Emwas, O. Shekhah, H. N. Alshareef and M. Eddaoudi, Covalent Organic Frameworks as Negative Electrodes for High-Performance Asymmetric Supercapacitors, *Adv. Energy Mater.*, 2020, **10**, 2001673, DOI: 10.1002/aenm.202001673.

70 M. A. Khayum, V. Vijayakumar, S. Karak, S. Kandambeth, M. Bhadra, K. Suresh, N. Acharambath, S. Kurungot and R. Banerjee, Convergent Covalent Organic Framework Thin Sheets as Flexible Supercapacitor Electrodes, *ACS Appl. Mater. Interfaces*, 2018, **10**, 28139–28146, DOI: 10.1021/acsami.8b10486.

71 X. Xu, T. Li, R. Zhang, Z. Zhang, W. Cao, Y. Wang, Y. Hu, X. Liu and S. Qiao, Covalent Organic Framework Nanofilm Heterojunctions: Lamination Effect and Suppressed Self-Discharge in Flexible Micro-Supercapacitors Energy Storage, *Small*, 2026, **22**(12), 2412642, DOI: 10.1002/smll.202412642.

72 Z. Peng, Y. He, N. Li, Z. Feng, Y. Chang, X. Shi, X. Meng, Z. Yan, M. Lu and K. Xu, Snowflake pores enhance energy storage in hcb-COF supercapacitors: Molecular dynamics insights into shape-dependent charging, *J. Mol. Liq.*, 2025, **430**, 127764, DOI: 10.1016/j.molliq.2025.127764.

73 N. Dhama, K. Singh and D. T. Masram, Rational design of a novel COF/GO (Tp-BDMe2/GO) hybrid composite for superior performance of a supercapacitor electrode, *J. Alloys Compd.*, 2025, **1043**, 184272, DOI: 10.1016/j.jallcom.2025.184272.

74 Z. Zhang, X. Xu, X. Xing, X. Tang, X. Zhang, J. Chen, Y. Xu and H. Jiang, Exquisitely functionalized porphyrin-COF self-supporting nanofilm for high-performance in-plane micro-supercapacitor, *Appl. Surf. Sci.*, 2025, **680**, 161327, DOI: 10.1016/j.apsusc.2024.161327.

75 C. F. Molla, B. B. Gicha, B. F. Banti, I. M. Khoris and J. Lee, Built-In Interfacial Electric Field in Hydroxyl-Terminated MXene/COF Heterostructures for Enhanced Solid-State Supercapacitors, *Adv. Funct. Mater.*, 2026, e75188, DOI: 10.1002/adfm.75188.

76 H. N. Abdelhamid, Tailoring Porosity and CO2 Capture Performance of Covalent Organic Frameworks Through Hybridization with Two-Dimensional Nanomaterials, *Inorganics*, 2025, **13**, 237, DOI: 10.3390/inorganics13070237.

77 M. G. Schwab, B. Fassbender, H. W. Spiess, A. Thomas, X. Feng and K. Müllen, Catalyst-free Preparation of Melamine-Based Microporous Polymer Networks through Schiff Base Chemistry, *J. Am. Chem. Soc.*, 2009, **131**, 7216–7217, DOI: 10.1021/ja902116f.

78 A. A. Sadek, M. Abd-Elkareem, H. N. Abdelhamid, S. Moustafa and K. Hussein, Enhancement of critical-sized bone defect regeneration using UiO-66 nanomaterial in rabbit femurs, *BMC Vet. Res.*, 2022, **18**, 260, DOI: 10.1186/s12917-022-03347-9.

79 H. N. Abdelhamid, Solid Acid Zirconium Oxo Sulfate/Carbon-Derived UiO-66 for Hydrogen Production, *Energy Fuels*, 2021, **35**, 10322–10326, DOI: 10.1021/acs.energyfuels.1c00516.

80 W. Sharmoukh, Z. M. Hassan, S. G. Mohamed and H. N. Abdelhamid, Metal-organic frameworks (UiO66-NH2)/PEDOT-derived ZrO2/N, S-doped carbon for supercapacitors, *J. Energy Storage*, 2024, **102**, 114071, DOI: 10.1016/j.est.2024.114071.

81 A. R. Heiba, M. O. Abdel-Salam, T. Yoon and E. El Sawy, Zr-MOF composites with zipped and unzipped carbon nanotubes for high-performance electrochemical supercapacitors, *Nanoscale*, 2025, **17**, 459–473, DOI: 10.1039/D4NR03926B.

82 K. Jayaramulu, M. Horn, A. Schneemann, H. Saini, A. Bakandritsos, V. Ranc, M. Petr, V. Stavila, C. Narayana, B. Scheibe, Š. Kment, M. Otyepka, N. Motta, D. Dubal, R. Zbořil and R. A. Fischer, Covalent Graphene-MOF Hybrids for High-Performance Asymmetric Supercapacitors, *Adv. Mater.*, 2021, **33**(4), 2004560, DOI: 10.1002/adma.202004560.

83 Y. Chen, X. Xie, J. Jing, Y. Wang, D. Cui, D. Liu and C. Xue, High-voltage planar supercapacitors enabled by Mn-MOF and ionic liquid synergy for high energy-density storage, *Electrochim. Acta*, 2025, **532**, 146494, DOI: 10.1016/j.electacta.2025.146494.